47th AIAA/ASME/SAE/ASEE Joint Propulsion Conference & Exhibit
31 July - 03 August 2011, San Diego, California

AIAA 2011-5692

On the Viscous Bidirectional Vortex with Arbitrary Endwall Injection

Georges Akiki* and Joseph Majdalani†
University of Tennessee Space Institute, Tullahoma, TN 37388

This work extends the inviscid framework developed by the authors for the purpose of modeling swirl-dominated cyclonic motions in straight cylindrical chambers with arbitrarily specified endwall velocities (Akiki, G. and Majdalani, J., "On the Bidirectional Vortex with Arbitrary Endwall Velocity," AIAA Paper 2010-6652, July 2010). This framework emerges directly from the Bragg-Hawthorne streamfunction equation and leads to an exact Euler solution that is capable of reproducing the flow in a bidirectional vortex chamber under a variety of user-prescribed inlet and outlet conditions. However, being derived in a frictionless environment, it leads to a characteristic singularity along the axis of rotation that affects both tangential velocity and pressure. The unbounded behavior of some properties about the centerline may be linked to the presence of a forced vortex in the core region that cannot be captured in a viscosity-free setting. The present study will overcome this deficiency by first transforming the tangential momentum equation with viscous diffusion to a form that is more germane to the core boundary layer region. Then using the tools of matched asymptotic expansions, a stretched radial coordinate is introduced to the extent of producing an inner velocity approximation that can be smoothly matched to the outer, inviscid flowfield. The latter manifests itself in an essentially free vortex that remains nearly invariant in the axial direction. By superimposing the inner and outer solutions asymptotically, a singularity-free representation is obtained for the swirl velocity, vorticity, and pressure. In the process, our analysis reveals a new dimensionless parameter, the generalized vortex Reynolds number; this group parameter incorporates the viscous Reynolds number, swirl number, aspect ratio, and imposed velocity pattern. We also find that vorticity originating from the viscous core markedly exceeds the vorticity introduced at the boundary as a result of fluid injection. Finally, all properties are discussed and compared to their inviscid counterparts.

Nomenclature

a = chamber radius
B = tangential angular momentum, ru_θ
b = chamber outlet radius
C = tangential momentum constant

*Graduate Research Assistant, Mechanical, Aerospace and Biomedical Engineering Department. Member AIAA, ASME.
†H. H. Arnold Chair of Excellence in Advanced Propulsion, Mechanical, Aerospace and Biomedical Engineering Department. Associate Fellow AIAA. Fellow ASME.

D = tangential surface parameter
K = bidirectional swirl number inverted, V_g / Re , given by Eq. (21)
L = chamber length
l = chamber aspect ratio, L / a
Re = injection Reynolds number, Ua / v
s = scaled radial coordinate
U = mean tangential (inflow) velocity
$U_0(r)$ = arbitrary axial velocity at the headwall
$U_L(r)$ = arbitrary axial velocity at the endwall
u_r = dimensional radial velocity
u_θ = dimensional tangential velocity
u_z = dimensional axial velocity
V_g = generalized vortex Reynolds number, given by Eqs. (31)–(34)
z, r, θ = axial, radial and tangential coordinates

Greek
ε = viscous parameter
κ = tangential inflow parameter, $(2\pi\sigma l)^{-1}$
λ_n = nth zero of J_1, the Bessel function of the first kind
ν = dynamic viscosity
σ = swirl number
υ = separation constant
ω = vorticity
ω_f = angular velocity
ψ = stream function

Superscripts
$\bar{}$ = overbars denote a nondimensional variable
c = composite solution
cl = common limit
i = inner solution
o = outer solution

I. Introduction

VORTEX flows have been a fascination to science since early recorded history. From the irrotational vortex paradox to the galactic pinwheels forming our universe, the emergence of large-scale vortex structures in several naturally occurring phenomena, such as tornadoes and hurricanes, has often triggered keen interest amongst researchers. Perhaps the earliest description of such phenomena can be found in early Greek methodology, mainly in Homer's Odyssey, where a vivid account is given of *Charybdis*,[1] a sea monster who, according to explorers and navigators, manifested itself in the form of an unpredictable whirlpool.

The introduction of rotating flows to the propulsion community may have started at the CSTAR facility of the University of Tennessee Space Institute in the early nineties, with Gloyer, Knuth and Goodman[2] and their unidirectional Vortex Hybrid Engine experiment. Knuth *et al.*[3] then went on to conceive the bidirectional Vortex Injection Hybrid Rocket Engine, followed by the Vortex Combustion Cold-Wall Chamber developed by Chiaverini *et al.*,[4] and the Reverse Vortex Combustor designed by Matveev *et al.*[5] Some of these studies are described in a paper by Majdalani.[6]

Prior to their connection with rocket engines, cyclonic flow investigations have been primarily confined to industrial applications. One of the earliest studies reported to-date may be traced back to Rankine[7] and the work in which he separated the tangential velocity of a vortex into a free and a forced motion. Studies by Oseen,[8] Lamb,[9] and Batchelor[10] followed Rankine's and provided marked improvements in dimensionality and modeling capability. For example, the Lamb-Oseen vortex was made to incorporate shear and therefore temporal decay. Conversely, the Burgers-Rott[11,12] model produced a vortex pattern that was spatially dependent, unlike the Lamb-Oseen vortex that was solely time-dependent.

Skimming through available surveys on the subject, it may be safe to state that considerably fewer models that pertain to bidirectional vortex motion may be spotted in the literature. The first to present an exact solution for similar flowfields was perhaps Sullivan[13] with his two-cell vortex; this was followed by Bloor and Ingham[14] whose work was extended by Barber and Majdalani.[15] For the interested reader, a recent survey of the advancements in modeling confined vortexes is available.[16]

In parallel to the theoretical modeling efforts toward vortex-dominated flows, several experiments such as the ones by Kelsall[17] and Smith[18,19] have been conducted to better understand the behavior of swirling motions. Comparably pertinent numerical investigations have been performed, including those by: Hoekstra, Derksen and van den Akker,[20] Derksen and van den Akker,[21] Fang, Majdalani and Chiaverini,[22] and Rom, Anderson and Chiaverini.[23]

Given the shortage of purely analytical models of axisymmetric cyclonic flows, an Eulerian-based solution, known as the complex-lamellar profile, was developed successively by Vyas and Majdalani[24] and, in spherical coordinates, by Majdalani and Rienstra.[25] The inviscid model, by analogy to that of Bloor and Ingham,[14] displayed a singularity at the centerline where the presence of a forced vortex core could not be captured in the absence of shear. In a remedial action, both core and sidewall viscous corrections in the azimuthal direction were introduced to the complex-lamellar model by Majdalani and Chiaverini.[26] Batterson and Majdalani[27] then added the sidewall no slip for the radial and axial components, thereby accomplishing a uniformly valid, *ad hoc* solution over the majority of the chamber domain.

Soon after in 2009, a study by Majdalani[6] presented a set of exact inviscid solutions for the bidirectional vortex flowfield using the incompressible Bragg-Hawthorne equation as a starting point. This work also showed how these helical profiles could be extended to the realm of hybrid engine analysis by adding sidewall injection.

In an effort to extend the 2009 monograph, a more general framework was recently developed by Akiki and Majdalani.[28] The new formulation combines all possible solutions reported by Majdalani[6] into a powerful Fourier-like series that seems capable of accommodating an arbitrary inlet or outlet velocity pattern. In accordance with the theory of inviscid swirling flow, the ensuing Euler solution is also found to exhibit a subtle singularity at the origin, namely, one that affects the swirling speed and its derivatives, such as the pressure distribution, near the axis of rotation.

In this paper, a similar approach to that used by Majdalani and Chiaverini[26] will be applied to first regularize the momentum equation and, second, remove the singularity encountered in the preceding work.[28] The physical setting,

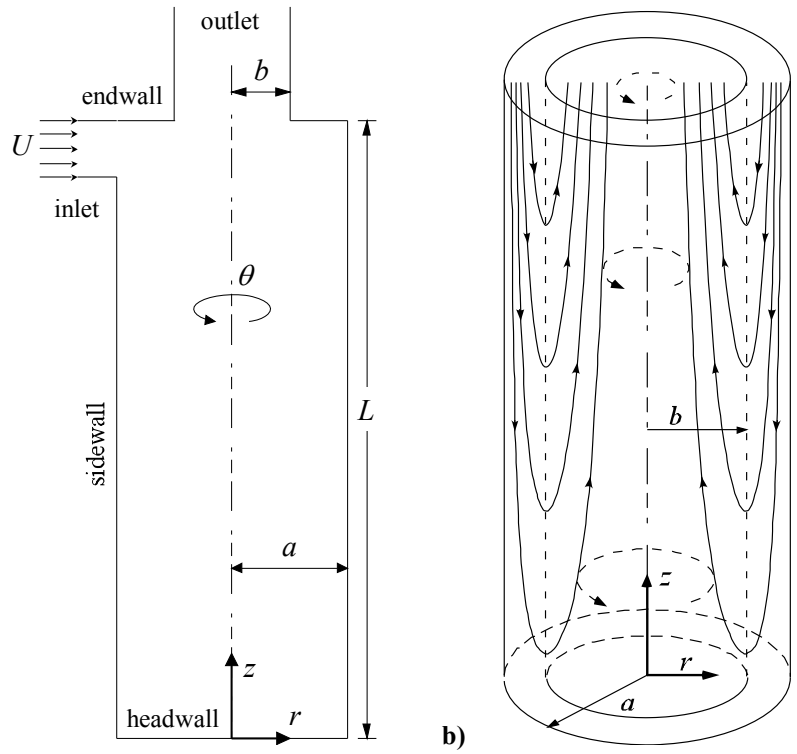

Figure 1. Schematic of a cyclonic chamber showing a) separate vortex regions and b) coordinate system used.

geometric configuration and coordinates used will remain unchanged, as given in Fig. 1. The objective will consist of producing a uniformly valid approximation for $0 \le r < a$, with a forced viscous core approximation, and the ability to incorporate an arbitrary endwall velocity.

II. Mathematical Procedure

The equations of motion for steady axisymmetric inviscid flow of an incompressible fluid are:

$$u_z \frac{\partial u_z}{\partial z} + u_r \frac{\partial u_z}{\partial r} = -\frac{1}{\rho}\frac{\partial p}{\partial z} \tag{1}$$

$$u_z \frac{\partial u_r}{\partial z} + u_r \frac{\partial u_r}{\partial r} - \frac{u_\theta^2}{r} = -\frac{1}{\rho}\frac{\partial p}{\partial r} \tag{2}$$

$$u_z \frac{\partial u_\theta}{\partial z} + u_r \frac{\partial u_\theta}{\partial r} + \frac{u_\theta u_r}{r} = 0 \tag{3}$$

This set is coupled with the continuity equation which can be written as:

$$\frac{\partial u_z}{\partial z} + \frac{1}{r}\frac{\partial (r u_r)}{\partial r} = 0 \tag{4}$$

Solving the above equation leads to an exact inviscid solution, as shown in previous work by the authors.[28] This solution is dominant in the outer region. Its normalized velocity components are:

$$\bar{u}_z(\bar{r},\bar{z}) = \sum_{n=0}^{k}\left[\frac{\bar{I}_l - \cos(\bar{\upsilon}_n l)\bar{I}_0}{\lambda_n J_0^2(\lambda_n)\sin(\bar{\upsilon}_n l)}\sin(\bar{\upsilon}_n \bar{z}) + \frac{\bar{I}_0 \cos(\bar{\upsilon}_n \bar{z})}{\lambda_n J_0^2(\lambda_n)}\right] J_0(\lambda_n \bar{r})$$
$$+ \sum_{n=k+1}^{\infty}\left[\frac{\bar{I}_l - \cosh(\bar{\upsilon}_n^* l)\bar{I}_0}{\lambda_n J_0^2(\lambda_n)\sinh(\bar{\upsilon}_n^* l)}\sinh(\bar{\upsilon}_n^* \bar{z}) + \frac{\bar{I}_0 \cosh(\bar{\upsilon}_n^* \bar{z})}{\lambda_n J_0^2(\lambda_n)}\right] J_0(\lambda_n \bar{r}) \tag{5}$$

$$\bar{u}_r(\bar{r},\bar{z}) = -\sum_{n=0}^{k}\left[\frac{\bar{I}_l - \cos(\bar{\upsilon}_n l)\bar{I}_0}{\lambda_n J_0^2(\lambda_n)\sin(\bar{\upsilon}_n l)}\bar{\upsilon}_n \cos(\bar{\upsilon}_n \bar{z}) - \frac{\bar{I}_0 \bar{\upsilon}_n \sin(\bar{\upsilon}_n \bar{z})}{\lambda_n J_0^2(\lambda_n)}\right] J_1(\lambda_n \bar{r})$$
$$-\sum_{n=k+1}^{\infty}\left[\frac{\bar{I}_l - \cosh(\bar{\upsilon}_n^* l)\bar{I}_0}{\lambda_n J_0^2(\lambda_n)\sinh(\bar{\upsilon}_n^* l)}\bar{\upsilon}_n^* \cosh(\bar{\upsilon}_n \bar{z}) + \frac{\bar{I}_0 \bar{\upsilon}_n^* \sinh(\bar{\upsilon}_n^* \bar{z})}{\lambda_n J_0^2(\lambda_n)}\right] J_1(\lambda_n \bar{r}) \tag{6}$$

and

$$\bar{u}_\theta(\bar{r},\bar{z}) = \left(\bar{C}^2\left\{\sum_{n=0}^{k}\left[\frac{\bar{I}_l - \cos(\bar{\upsilon}_n l)\bar{I}_0}{\lambda_n J_0^2(\lambda_n)\sin(\bar{\upsilon}_n l)}\sin(\bar{\upsilon}_n \bar{z}) + \frac{\bar{I}_0 \cos(\bar{\upsilon}_n \bar{z})}{\lambda_n J_0^2(\lambda_n)}\right] J_1(\lambda_n \bar{r})\right.\right.$$
$$\left.\left. + \sum_{n=k+1}^{\infty}\left[\frac{\bar{I}_l - \cosh(\bar{\upsilon}_n^* l)\bar{I}_0}{\lambda_n J_0^2(\lambda_n)\sinh(\bar{\upsilon}_n^* l)}\sinh(\bar{\upsilon}_n^* \bar{z}) + \frac{\bar{I}_0 \cosh(\bar{\upsilon}_n^* \bar{z})}{\lambda_n J_0^2(\lambda_n)}\right] J_1(\lambda_n \bar{r})\right\}^2 + \frac{\bar{D}}{\bar{r}^2}\right)^{\frac{1}{2}} \tag{7}$$

where

$$\begin{cases} \bar{I}_l \equiv 2\int_0^1 \bar{u}_z(\bar{r},l)\bar{r}J_0(\lambda_n \bar{r})\,\mathrm{d}\bar{r} & \text{(endwall)} \\ \bar{I}_0 \equiv 2\int_0^1 \bar{u}_z(\bar{r},0)\bar{r}J_0(\lambda_n \bar{r})\,\mathrm{d}\bar{r} & \text{(headwall)} \end{cases} \tag{8}$$

and

$$\begin{cases} \bar{\upsilon}_n = \sqrt{\bar{C}^2 - \lambda_n^2} \\ \bar{\upsilon}_n^* = \sqrt{\lambda_n^2 - \bar{C}^2} \end{cases} \tag{9}$$

The corresponding streamfunction is given by

$$\bar{\psi}(\bar{r},\bar{z}) = \sum_{n=0}^{k}\bar{r}\left[\frac{\bar{I}_L - \cos(\bar{\upsilon}_n l)\bar{I}_0}{\lambda_n J_0^2(\lambda_n)\sin(\bar{\upsilon}_n l)}\sin(\bar{\upsilon}_n \bar{z}) + \frac{\bar{I}_0 \cos(\bar{\upsilon}_n \bar{z})}{\lambda_n J_0^2(\lambda_n)}\right] J_1(\lambda_n \bar{r})$$
$$+\sum_{n=k+1}^{\infty} r\left[\frac{\bar{I}_L - \cosh(\bar{\upsilon}_n^* l)\bar{I}_0}{\lambda_n J_0^2(\lambda_n)\sinh(\bar{\upsilon}_n^* l)}\sinh(\bar{\upsilon}_n^* \bar{z}) + \frac{\bar{I}_0 \cosh(\bar{\upsilon}_n^* \bar{z})}{\lambda_n J_0^2(\lambda_n)}\right] J_1(\lambda_n \bar{r}) \tag{10}$$

The non-dimensional forms of the variables are specified consistently with previous work.[28] Using standard reference values, we set

$$\begin{cases} \bar{r} = \dfrac{r}{a},\ \bar{z} = \dfrac{z}{a},\ \bar{u}_r = \dfrac{u_r}{U},\ \bar{u}_z = \dfrac{u_z}{U},\ \bar{u}_\theta = \dfrac{u_\theta}{U} \\ \bar{\psi} = \dfrac{\psi}{Ua^2},\ \bar{D} = \dfrac{D}{U^2 a^2},\ \bar{C} = Ca,\ \bar{p} = \dfrac{p}{\rho U^2} \end{cases} \tag{11}$$

A. Tangential Viscous Correction

The last term in Eq. (7) leads to a singularity at the centerline when $\bar{D} \neq 0$. This is due to the inviscid assumption and seems to be an ubiquitous characteristic of swirl-dominated motions.[14]

The mechanisms that will force the tangential velocity at the centerline to vanish, instead of growing continuously to unbounded levels, are connected to the viscous stresses. To account for their presence, one must retain the viscous term in the tangential momentum equation, thus leading to a regularized form to start with:

$$\bar{u}_z\frac{\partial \bar{u}_\theta}{\partial \bar{z}} + \bar{u}_r\frac{\partial \bar{u}_\theta}{\partial \bar{r}} + \frac{\bar{u}_\theta \bar{u}_r}{\bar{r}} = \frac{1}{Re}\frac{\partial}{\partial \bar{r}}\left[\frac{1}{\bar{r}}\frac{\partial(\bar{r}\bar{u}_\theta)}{\partial \bar{r}} + \frac{\partial^2 \bar{u}_\theta}{\partial \bar{z}^2}\right] \tag{12}$$

Here the Reynolds number is based on the tangential reference velocity U and the chamber radius a,

$$Re = \frac{\rho U a}{\mu} \tag{13}$$

B. Core Solution

By solving Eq. (12) for the region close to the centerline, the result can be paired with the outer, inviscid solution, to produce a uniformly valid approximation over the domain extending from the centerline up to but excluding the sidewall. In practical applications, the Reynolds number corresponding to vortex-fired engines appears at orders greater than 10^3. This justifies the use of the small perturbation parameter ε, where

$$\varepsilon = \frac{1}{Re} \tag{14}$$

At this juncture, it may be instructive to note that based on several experimental observations[18,19] and inviscid models previously reported,[6,24] the spatial dependence of the tangential velocity on the axial position may be assumed to be secondary. This prompts us to take:

$$\frac{\partial \overline{u}_\theta}{\partial z} = 0 \tag{15}$$

Based on Eqs. (14) and (15), Eq. (12) reduces to

$$\varepsilon \frac{\mathrm{d}}{\mathrm{d}\overline{r}}\left[\frac{1}{\overline{r}}\frac{\mathrm{d}\overline{B}(\overline{r},\overline{z})}{\mathrm{d}\overline{r}}\right] - \frac{\overline{u}_r}{\overline{r}}\frac{\mathrm{d}\overline{B}(\overline{r},\overline{z})}{\mathrm{d}\overline{r}} = 0 \tag{16}$$

where

$$\overline{B}(\overline{r},\overline{z}) = \overline{r}\overline{u}_\theta \tag{17}$$

To suitably capture the rapid changes that occur in the core region, stretching of the domain is required, and this can be accomplished through a coordinate transformation of the type:

$$\overline{s} = \frac{\overline{r}}{\delta(\varepsilon)} \tag{18}$$

Moreover, the Bessel function embedded in the radial velocity term can be expanded using a Taylor series that renders

$$J_1(\lambda_n \delta \overline{s}) = \frac{\overline{s}\lambda_n}{2}\delta - \frac{\overline{s}^3\lambda_n^3}{16}\delta^3 + \ldots \tag{19}$$

When Eq. (19) is inserted into Eq. (16), further simplifications lead to

$$\frac{\varepsilon}{\delta^2}\frac{\mathrm{d}^2\overline{B}(\overline{s},\overline{z})}{\mathrm{d}\overline{s}^2} + \frac{\overline{s}}{2}K\frac{\mathrm{d}\overline{B}(\overline{s},\overline{z})}{\mathrm{d}\overline{s}} - \frac{\varepsilon}{\delta^2\overline{s}}\frac{\mathrm{d}\overline{B}(\overline{s},\overline{z})}{\mathrm{d}\overline{s}} = 0 \tag{20}$$

where

$$K(\overline{z}) = \sum_{n=0}^{k}\left[\frac{\overline{I}_l - \cos\left(\overline{\upsilon}_n l\right)\overline{I}_0}{\lambda_n J_0^2\left(\lambda_n\right)\sin\left(\overline{\upsilon}_n l\right)}\overline{\upsilon}_n\cos\left(\overline{\upsilon}_n\overline{z}\right) - \frac{\overline{I}_0\overline{\upsilon}_n\sin\left(\overline{\upsilon}_n\overline{z}\right)}{\lambda_n J_0^2\left(\lambda_n\right)}\right]\lambda_n$$
$$+ \sum_{n=k+1}^{\infty}\left[\frac{\overline{I}_l - \cosh\left(\overline{\upsilon}_n^* l\right)\overline{I}_0}{\lambda_n J_0^2\left(\lambda_n\right)\sinh\left(\overline{\upsilon}_n^* l\right)}\overline{\upsilon}_n^*\cosh\left(\overline{\upsilon}_n\overline{z}\right) + \frac{\overline{I}_0\overline{\upsilon}_n^*\sinh\left(\overline{\upsilon}_n^*\overline{z}\right)}{\lambda_n J_0^2\left(\lambda_n\right)}\right]\lambda_n \tag{21}$$

A proper scaling can then be chosen such that $\varepsilon/\delta^2 = O(1)$; the distinguished limit becomes

$$\delta(\varepsilon) \approx \sqrt{\varepsilon} \tag{22}$$

Taking $\delta = \sqrt{\varepsilon}$, the ODE to solve reduces to

$$\frac{\mathrm{d}^2\overline{B}(\overline{s},\overline{z})}{\mathrm{d}\overline{s}^2} + \frac{\overline{s}}{2}K\frac{\mathrm{d}\overline{B}(\overline{s},\overline{z})}{\mathrm{d}\overline{s}} - \frac{1}{\overline{s}}\frac{\mathrm{d}\overline{B}(\overline{s},\overline{z})}{\mathrm{d}\overline{s}} = 0 \tag{23}$$

for which a solution may be obtained in the form

$$\overline{B}^{(i)}(\overline{s},\overline{z}) = \frac{C_1}{K}\exp\left(-\tfrac{1}{4}K\overline{s}^2\right) + C_2 \tag{24}$$

The two constants C_1 and C_2 must be determined from the physical requirement at the core and matching with the outer, invsicid velocity.

C. Boundary Conditions and Asymptotic Matching

To permit the establishment of a forced vortex core, the first boundary condition requires constraining the tangential velocity to vanish at $\bar{r}=0$. This implies that

$$\bar{u}_\theta(0)=0,\ \bar{B}(0)=0,\quad \text{and}\quad \frac{C_1}{K}+C_2=0 \tag{25}$$

Prandtl's Matching Principle can then be applied to promote matching between the inner approximation and the outer inviscid solution given earlier by Eq. (7). This principle can be implemented by setting

$$\lim_{\bar{s}\to\infty}\bar{u}_\theta^{(i)}=\lim_{\bar{r}\to 0}\bar{u}_\theta^{(o)}=\bar{u}_\theta^{(cl)} \tag{26}$$

where $\bar{u}_\theta^{(cl)}$ represents the common limit. This equality ensures that the outer limit of the inner velocity is led to perform identically to the inner limit of the outer inviscid solution.

From Eqs. (25) and (26), the two constants C_1 and C_2 may be fully determined. The final inner solution becomes

$$u_\theta^{(i)}=-\frac{\sqrt{\bar{D}}}{\bar{r}}\exp\left(-\tfrac{1}{4}KRe\,\bar{r}^2\right)+\frac{\sqrt{\bar{D}}}{\bar{r}} \tag{27}$$

To produce a solution that is uniformly valid over the entire domain (except for the walls), the inner and outer approximations must be combined to form what is known as the composite solution; this is achieved by summing

$$\bar{u}_\theta^{(c)}=\bar{u}_\theta^{(o)}+\bar{u}_\theta^{(i)}-\bar{u}_\theta^{(cl)} \tag{28}$$

whence

$$\bar{u}_\theta^{(c)}=\left(\bar{C}^2\left\{\sum_{n=0}^{k}\left[\frac{\bar{I}_l-\cos\left(\bar{\upsilon}_n l\right)\bar{I}_0}{\lambda_n a J_0^2\left(\lambda_n\right)\sin\left(\bar{\upsilon}_n l\right)}\sin\left(\bar{\upsilon}_n\bar{z}\right)+\frac{\bar{I}_0\cos\left(\bar{\upsilon}_n\bar{z}\right)}{\lambda_n a J_0^2\left(\lambda_n\right)}\right]J_1\left(\lambda_n\bar{r}\right)\right.\right.$$
$$\left.\left.+\sum_{n=k+1}^{\infty}\left[\frac{\bar{I}_l-\cosh\left(\bar{\upsilon}_n^* l\right)\bar{I}_0}{\lambda_n J_0^2\left(\lambda_n\right)\sinh\left(\bar{\upsilon}_n^* l\right)}\sinh\left(\bar{\upsilon}_n^*\bar{z}\right)+\frac{\bar{I}_0\cosh\left(\bar{\upsilon}_n^*\bar{z}\right)}{\lambda_n J_0^2\left(\lambda_n\right)}\right]J_1\left(\lambda_n\bar{r}\right)\right\}^2+\frac{\bar{D}}{\bar{r}^2}\right)^{\frac{1}{2}}-\frac{\sqrt{\bar{D}}}{\bar{r}}\exp\left(-\tfrac{1}{4}KRe\bar{r}^2\right) \tag{29}$$

Equation (29) represents the apex of this study. It consists of a pseudo-viscous model that is no longer singular at the centerline, but rather uniformly valid for $0\le\bar{r}<1$. It should be noted that the last member incorporates the effect of viscous attenuation near the core. As depicted by the solution, this part depends mainly on the product of the Reynolds number and K; the latter incorporates the source integrals $\bar{I}_0$ and $\bar{I}_l$ as well as the swirl number and aspect ratio of the chamber. At the outset, the viscous corrections will change with different boundary conditions and prescribed velocities at inlets and outlets.

The grouping of (KRe) plays the role of the vortex Reynolds number V reported by Majdalani and Chiaverini,[26] therein, it is written as

$$V=\frac{Re}{\sigma l} \tag{30}$$

In its native form, this parameter combines the effects of the Reynolds number, swirl number, and chamber aspect ratio. In the present generalization, the swirl number is imbedded within the boundary conditions and does not appear explicitly. Here too, K stands as a function of the chamber aspect ratio and swirl number. One may hence conceive of a generalized vortex Reynolds number from which V may be restored as a special case. This new dimensionless parameter bears the form

$$V_g = K\,Re = Re\left\{\sum_{n=0}^{k}\left[\frac{\bar{I}_l - \cos(\bar{\upsilon}_n l)\bar{I}_0}{\lambda_n J_0^2(\lambda_n)\sin(\bar{\upsilon}_n l)}\bar{\upsilon}_n\cos(\bar{\upsilon}_n\bar{z}) - \frac{\bar{I}_0\bar{\upsilon}_n\sin(\bar{\upsilon}_n\bar{z})}{\lambda_n J_0^2(\lambda_n)}\right]\lambda_n \right.$$
$$\left. + \sum_{n=k+1}^{\infty}\left[\frac{\bar{I}_l - \cosh(\bar{\upsilon}_n^* l)\bar{I}_0}{\lambda_n J_0^2(\lambda_n)\sinh(\bar{\upsilon}_n^* l)}\bar{\upsilon}_n^*\cosh(\bar{\upsilon}_n^*\bar{z}) + \frac{\bar{I}_0\bar{\upsilon}_n^*\sinh(\bar{\upsilon}_n^*\bar{z})}{\lambda_n J_0^2(\lambda_n)}\right]\lambda_n\right\} \tag{31}$$

Despite its apparent complexity, V_g is straightforward to evaluate. For the case of zero headwall injection, it reduces to

$$V_g = K\,Re = Re\left[\sum_{n=0}^{k}\frac{\bar{I}_l\bar{\upsilon}_n\cos(\bar{\upsilon}_n\bar{z})}{J_0^2(\lambda_n)\sin(\bar{\upsilon}_n l)} + \sum_{n=k+1}^{\infty}\frac{\bar{I}_l\bar{\upsilon}_n^*\cosh(\bar{\upsilon}_n^*\bar{z})}{J_0^2(\lambda_n)\sinh(\bar{\upsilon}_n^* l)}\right] \tag{32}$$

Furthermore, for the case of a single mode (such as the one corresponding to linear Beltramian injection at the endwall), the generalized vortex Reynolds number collapses first into

$$V_g = Re\bar{I}_l\frac{\bar{\upsilon}_0\cos(\bar{\upsilon}_0\bar{z})}{J_0^2(\lambda_0)\sin(\bar{\upsilon}_0 l)} \quad \text{or} \quad V_g = \frac{Re}{l}\frac{\bar{I}_l}{J_0^2(\lambda_0)}\frac{\bar{\upsilon}_0 l}{\sin(\bar{\upsilon}_0 l)}\cos(\bar{\upsilon}_0\bar{z}) \tag{33}$$

Second, it may be recognized that for flow matching to be realized at the endwall, one must roughly take $\bar{C}\approx\lambda_0$; this leaves us with the crude approximations of $\bar{\upsilon}_0\approx\sqrt{\bar{C}^2-\lambda_0^2}\approx 0$ and $\cos(\bar{\upsilon}_0\bar{z})\approx 1$. Plugging these back-of-the-envelope estimates into Eq. (33), we arrive at

$$V_g = \frac{Re\bar{I}_l}{J_0^2(\lambda_0)l} = \frac{Re\lambda_0\left[\kappa c l J_0^2(\lambda_0)\right]}{J_0^2(\lambda_0)l} = \frac{Re}{\sigma l}\left(\frac{c\lambda_0}{2\pi}\right) \quad \text{or} \quad V_g = \frac{Re}{\sigma l}(\text{const}) \tag{34}$$

We thus restore the original vortex Reynolds number[26] to within a constant. In the above, Eq. (8) is employed in the evaluation of $\bar{I}_l$; for the linear Beltramian motion, this integral can be obtained from

$$\bar{I}_l \equiv 2\int_0^1 \bar{u}_z(\bar{r},l)\bar{r}J_0(\lambda_0\bar{r})\,\mathrm{d}\bar{r} = 2\int_0^1\lambda_0 c\kappa l J_0^2(\lambda_0\bar{r})\bar{r}\,\mathrm{d}\bar{r} = \lambda_0 c\kappa l\left[J_0^2(\lambda_0)+J_1^2(\lambda_0)\right] = \lambda_0 c\kappa l J_0^2(\lambda_0) \tag{35}$$

where $J_1^2(\lambda_0)=0$ because λ_0 is the first zero of $J_1(x)=0$.

It should be noted that as $Re\to\infty$, $\bar{u}_\theta^{(c)}\to\bar{u}_\theta^{(o)}$, and the outer solution is readily restored. Conversely, as $\bar{r}\to 0$ at fixed Reynolds number, Eq. (29) can be expanded into

$$\bar{u}_\theta^{(c)} = \frac{\sqrt{\bar{D}}}{\bar{r}}\left[1-\exp\left(-\tfrac{1}{4}K\,Re\,\bar{r}^2\right)\right] = \frac{\sqrt{\bar{D}}}{4}K\,Re\,\bar{r} + O(\bar{r}^3) \tag{36}$$

Equation (36) demonstrates the ability of the solution to vanish at $\bar{r}=0$, thus securing the forced vortex requirment along the axis of rotation. It also reveals the linear relation between the tangential velocity and circular frequency of the forced vortex, which is known to undergo solid body rotation. This expression is $\bar{u}_\theta^{(c)}=\omega_f\bar{r}$, where ω_f denotes the angular speed of the core vortex. Clearly, it is given by:

$$\omega_f = \tfrac{1}{4}\sqrt{\bar{D}}K\,Re \tag{37}$$

For the Beltramian family of solutions considered here, we recall that $\bar{D}=1$, and so $\omega_f=\tfrac{1}{4}K\,Re=\tfrac{1}{4}V_g$. A similar result was previously reported by Majdalani and Chiaverini[22] and, using separate analysis, by Batterson and Majdalani.[29,30] Both groups found $\omega_f=\tfrac{1}{4}V$ in their characterization of the core layer in the complex-lamellar and Beltramian profiles, respectively.

D. Vorticity Correction

Another quantity of interest is the vorticity, $\bar{\boldsymbol{\omega}}=\nabla\times\bar{\boldsymbol{u}}$. Since we already have the components of $\bar{\boldsymbol{u}}$ defined in Eqs. (5), (6) and (29), the vorticity can be readily found via.

$$\bar{\omega}_r = -\frac{\bar{C}^2}{\bar{r}\sqrt{\bar{C}^2\bar{\psi}^2+\bar{D}}}\bar{\psi}\frac{\partial\bar{\psi}}{\partial\bar{z}} - \sqrt{\bar{D}}\frac{\mathrm{d}K}{\mathrm{d}\bar{z}}\frac{Re\bar{r}}{4}\exp\left(-\tfrac{1}{4}KRe\ \bar{r}^2\right) \tag{38}$$

where $\bar{\psi}$ is defined through Eq. (10) and, consequently,

$$\frac{\partial\bar{\psi}(\bar{r},\bar{z})}{\partial z} = \sum_{n=0}^{k}\bar{r}\left[\frac{\bar{I}_L-\cos(\bar{\upsilon}_n l)\bar{I}_0}{\lambda_n J_0^2(\lambda_n)\sin(\bar{\upsilon}_n l)}\bar{\upsilon}_n\cos(\bar{\upsilon}_n\bar{z}) - \frac{\bar{I}_0}{\lambda_n J_0^2(\lambda_n)}\bar{\upsilon}_n\sin(\bar{\upsilon}_n\bar{z})\right]J_1(\lambda_n\bar{r})$$
$$+\sum_{n=k+1}^{\infty} r\left[\frac{\bar{I}_L-\cosh(\bar{\upsilon}_n^* l)\bar{I}_0}{\lambda_n J_0^2(\lambda_n)\sinh(\bar{\upsilon}_n^* l)}\bar{\upsilon}_n^*\cosh(\bar{\upsilon}_n^*\bar{z}) + \frac{\bar{I}_0}{\lambda_n J_0^2(\lambda_n)}\bar{\upsilon}_n^*\sinh(\bar{\upsilon}_n^*\bar{z})\right]J_1(\lambda_n\bar{r}) \tag{39}$$

Then given Eq. (21), we have

$$\frac{\mathrm{d}K}{\mathrm{d}\bar{z}} = -\sum_{n=0}^{k}\left[\frac{\bar{I}_l-\cos(\bar{\upsilon}_n l)\bar{I}_0}{\lambda_n J_0^2(\lambda_n)\sin(\bar{\upsilon}_n l)}\bar{\upsilon}_n^{\,2}\sin(\bar{\upsilon}_n\bar{z}) - \frac{\bar{I}_0}{\lambda_n J_0^2(\lambda_n)}\bar{\upsilon}_n^{\,2}\cos(\bar{\upsilon}_n\bar{z})\right]\lambda_n$$
$$+\sum_{n=k+1}^{\infty}\left[\frac{\bar{I}_l-\cosh(\bar{\upsilon}_n^* l)\bar{I}_0}{\lambda_n J_0^2(\lambda_n)\sinh(\bar{\upsilon}_n^* l)}\bar{\upsilon}_n^{*2}\sinh(\bar{\upsilon}_n^*\bar{z}) + \frac{\bar{I}_0}{\lambda_n J_0^2(\lambda_n)}\bar{\upsilon}_n^{*2}\cosh(\bar{\upsilon}_n^*\bar{z})\right]\lambda_n \tag{40}$$

For the tangential component of vorticity, it may be evaluated from

$$\bar{\omega}_\theta = \frac{\bar{C}^2\bar{\psi}}{\bar{r}} \tag{41}$$

and, similarly, for the axial contribution, from

$$\bar{\omega}_z = \frac{\bar{C}^2}{\bar{r}\sqrt{\bar{C}^2\bar{\psi}^2+\bar{D}}}\bar{\psi}\frac{\partial\bar{\psi}}{\partial\bar{r}} + \frac{1}{2}\sqrt{\bar{D}}K\ Re\exp\left(-\tfrac{1}{4}K\ Re\ \bar{r}^2\right) \tag{42}$$

where

$$\frac{\partial\bar{\psi}}{\partial\bar{r}} = \sum_{n=0}^{k}\left[\frac{\bar{I}_L-\cos(\bar{\upsilon}_n l)\bar{I}_0}{\lambda_n J_0^2(\lambda_n)\sin(\bar{\upsilon}_n l)}\sin(\bar{\upsilon}_n\bar{z}) + \frac{\bar{I}_0}{\lambda_n J_0^2(\lambda_n)}\cos(\bar{\upsilon}_n\bar{z})\right]\left\{J_1(\lambda_n\bar{r}) + \frac{1}{2}\bar{r}[J_0(\lambda_n\bar{r}) - J_2(\lambda_n\bar{r})]\right\}$$
$$+\sum_{n=k+1}^{\infty}\left[\frac{\bar{I}_L-\cosh(\bar{\upsilon}_n^* l)\bar{I}_0}{\lambda_n J_0^2(\lambda_n)\sinh(\bar{\upsilon}_n^* l)}\sinh(\bar{\upsilon}_n^*\bar{z}) + \frac{\bar{I}_0}{\lambda_n J_0^2(\lambda_n)}\cosh(\bar{\upsilon}_n^*\bar{z})\right]\left\{J_1(\lambda_n\bar{r}) + \frac{1}{2}\bar{r}[J_0(\lambda_n\bar{r}) - J_2(\lambda_n\bar{r})]\right\} \tag{43}$$

The total vorticity becomes expressible through:

$$\bar{\omega} = \sqrt{\bar{\omega}_z^2 + \bar{\omega}_\theta^2 + \bar{\omega}_r^2} \tag{44}$$

The evaluation of $\bar{\omega}$ may be relegated to a symbolic program and is omitted here in the interest of brevity.

E. Pressure Correction

From the Euler momentum equations, it can be seen that the pressure gradient in the radial direction is dependent on the tangential velocity. The rectified form of $\bar{u}_\theta$ that incorporates the effects of friction near the core also leads to the removal of the singularity from the ensuing pressure distribution. This can be shown by examining the corrected pressure that may be extracted from:

$$-\frac{\partial\bar{p}^{(c)}}{\partial\bar{r}} = \bar{u}_z\frac{\partial\bar{u}_r}{\partial\bar{z}} + \bar{u}_r\frac{\partial\bar{u}_r}{\partial\bar{r}} - \frac{\left[\bar{u}_\theta^{(c)}\right]^2}{\bar{r}} \tag{45}$$

The axial and radial velocities used in Eq. (45) are the inviscid results given by Eqs. (5) and (6), respectively. These are still valid because no boundary layer exists in these directions near the centerline.

III. Results and Discussion

The introduction of viscosity into the tangential momentum has a substantial bearing on the swirl velocity, vorticity distribution, and pressure. These features are examined next.

A. Tangential Velocity

The swirl velocity distribution is defined through Eq. (29) where the last member on the right-hand-side represents the viscous correction. Evidently, this term is dependent on the Reynolds number given by Eq. (13). Figure 2 shows the variation of $\overline{u}_\theta$ at different axial positions, namely, $\overline{z} = 0.2,\ 0.4,\ 0.6,\ 0.8,\ 1$. It also lists the strictly inviscid model as a benchmark. Given that the present formulation only accounts for friction around the centerline, slip is permitted at $\overline{r} = 1$. At the outset, $\overline{u}_\theta$ at the sidewall matches the injection velocity $U_\theta(r)$, and then increases as it approaches the core region until it reaches a maximum $\overline{u}_{\theta\,\max}^{(c)}$. After peaking at $\overline{r} = \overline{r}_{\max}$ the swirl velocity diminishes down to its vanishing point along the centerline. The diameter consisting of $2\overline{r}_{\max}$ delineates the forced core region inside of which viscous elements dominate.

Figures 2a and b represent the variations at different axial positions for two different boundary conditions: the linear and the nonlinear Beltramian velocity distributions compiled by Majdalani.[6] Both have the same axial velocities at the boundary but dissimilar tangential velocity distributions. Particularly, the linear Beltramian profile entails a tangential momentum constant $\overline{C}$ of 3.828, whereas, in the nonlinear Beltramian case, $\overline{C} \approx 4.137$. The term in Eq. (29) that leads to axial dependency is $\overline{\upsilon}_n \cos \overline{\upsilon}_n \overline{z}$, and is explicitly embedded in K. Equation (9) shows that the term $\overline{\upsilon}_n$ must diminish as $\overline{C}$ approaches the eigenvalues λ_n. Since most of the weight in the summation series stems from its first term, it is sufficient for $\overline{C}$ to approach the first zero of the Bessel function of the first kind $(\lambda_1 = 3.832)$ to eliminate the dependency of the core tangential velocity on the axial position. This case is illustrated in Fig. 2a by the linear Beltramian endwall profile. In Fig. 2b, it may be seen that as the flow approaches the headwall, viscous effects in the nonlinear Beltramian model diminish with $\overline{z}$ to the extent of precipitating a nearly inviscid $\overline{u}_\theta^{(c)}$ near $\overline{z} = 0$.

In Fig. 3a, the sensitivity of $\overline{u}_\theta^{(c)}$ to different Reynolds numbers is illustrated. As *Re* increases, the core area decreases and inviscid conditions are nearly reproduced. For low swirl intensities, viscous effects stretch over a wider portion of the chamber and, while the core radius may be calculated by determining $\overline{r}_{\max}$ at which $\overline{u}_\theta^{(c)}$ reaches its peak value, no exact solution for $\overline{r}_{\max}$ may be realized. Instead, a root finding technique is used for this purpose. Results are summarized in Table 1 where the radius of the viscous core is quantified versus *Re* as predicted by the complex-lamellar viscous flowfield[26] side-by-side with the present solution whose inlet and outlet boundary

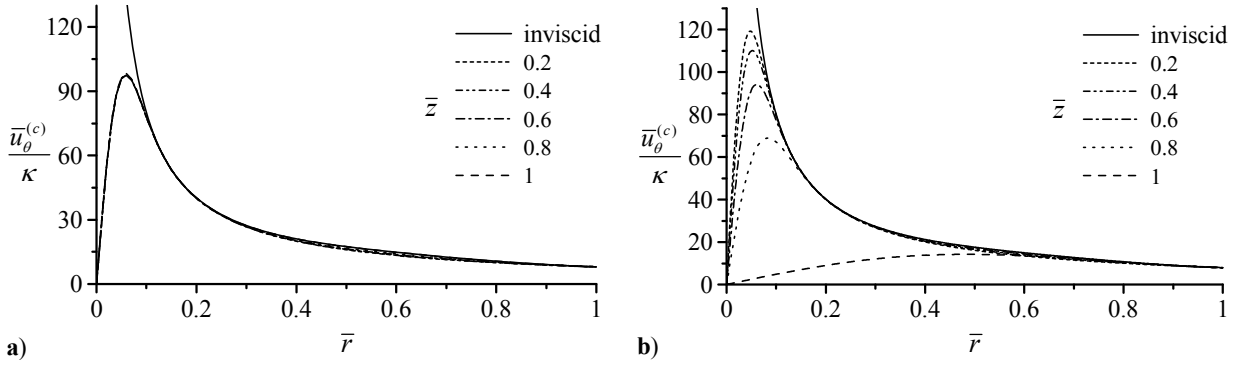

Figure 2. Tangential velocity at different axial positions for a) linear and b) nonlinear Beltramian base flows. Here *l* = 1, κ = 0.125 and *Re* = 1000.

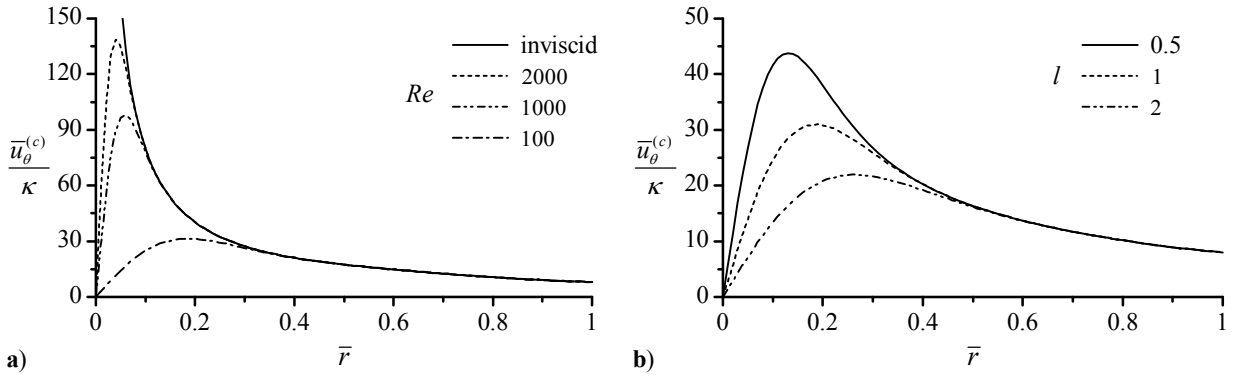

Figure 3. Tangential velocity for different a) Reynolds numbers and b) aspect ratios. Results feature the linear Beltramian inlet profile.

Table 1. Radial thickness of the viscous core for $\kappa = 0.125$ and $l = 1$

	$\overline{r}_{\max}$			
Re	**CL,[a] $\forall \overline{z}$**	**CL,[b] $\overline{z} = \frac{1}{2}l$**	**LB,[b] $\forall \overline{z}$**	**NB,[b] $\overline{z} = \frac{1}{2}l$**
2000	0.057	0.064	0.041	0.039
1500	0.065	0.074	0.048	0.045
1200	0.073	0.082	0.053	0.051
1000	0.080	0.090	0.058	0.056
500	0.113	0.128	0.083	0.079
200	0.179	0.202	0.131	0.124
100	0.253	0.286	0.186	0.176
50	0.358	0.404	0.264	0.252

[a]Original model.[26]

[b]Present solution with referenced models used at inlet; CL= complex-lamellar; LB: linear Beltramian; NB: nonlinear Beltramian.[6]

conditions are prescribed by the complex-lamellar (CL), linear Beltramian (LB) and nonlinear Beltramian (NB) models.

Further analysis of Eq. (29) reveals an interesting relation between the chamber aspect ratio and the size of the viscous region. To illustrate this point, Fig. 3b displays three plots of the tangential velocity at three different aspect ratios of $l = 0.5,\ 1,\ \text{and}\ 2$. Note that when l is increased, as in the case of elongated chambers, the role of viscous dissipation is magnified considerably, thus leading to a larger forced vortex region and lower swirl velocity throughout the chamber. This result confirms the study by Majdalani and Chiaverini.[26]

B. Rectified Vorticity Distribution

Figure 4 describes the vorticity distribution in the vortex chamber with and without viscosity. Parts a, b and c include viscosity in the core region and Part d corresponds to the strictly inviscid model; the latter is given by

$$\overline{\omega}^{(i)} = \sqrt{\left[\overline{\omega}_r^{(i)}\right]^2 + \left[\overline{\omega}_\theta^{(i)}\right]^2 + \left[\overline{\omega}_z^{(i)}\right]^2} \tag{46}$$

where

$$\overline{\omega}_r^{(i)} = -\frac{\overline{C}^2}{\overline{r}\sqrt{\overline{C}^2\overline{\psi}^2 + \overline{D}}}\overline{\psi}\frac{\partial \overline{\psi}}{\partial \overline{z}} \tag{47}$$

and

$$\overline{\omega}_z^{(i)} = \frac{\overline{C}^2}{\overline{r}\sqrt{\overline{C}^2\overline{\psi}^2 + \overline{D}}}\overline{\psi}\frac{\partial \overline{\psi}}{\partial \overline{r}} \tag{48}$$

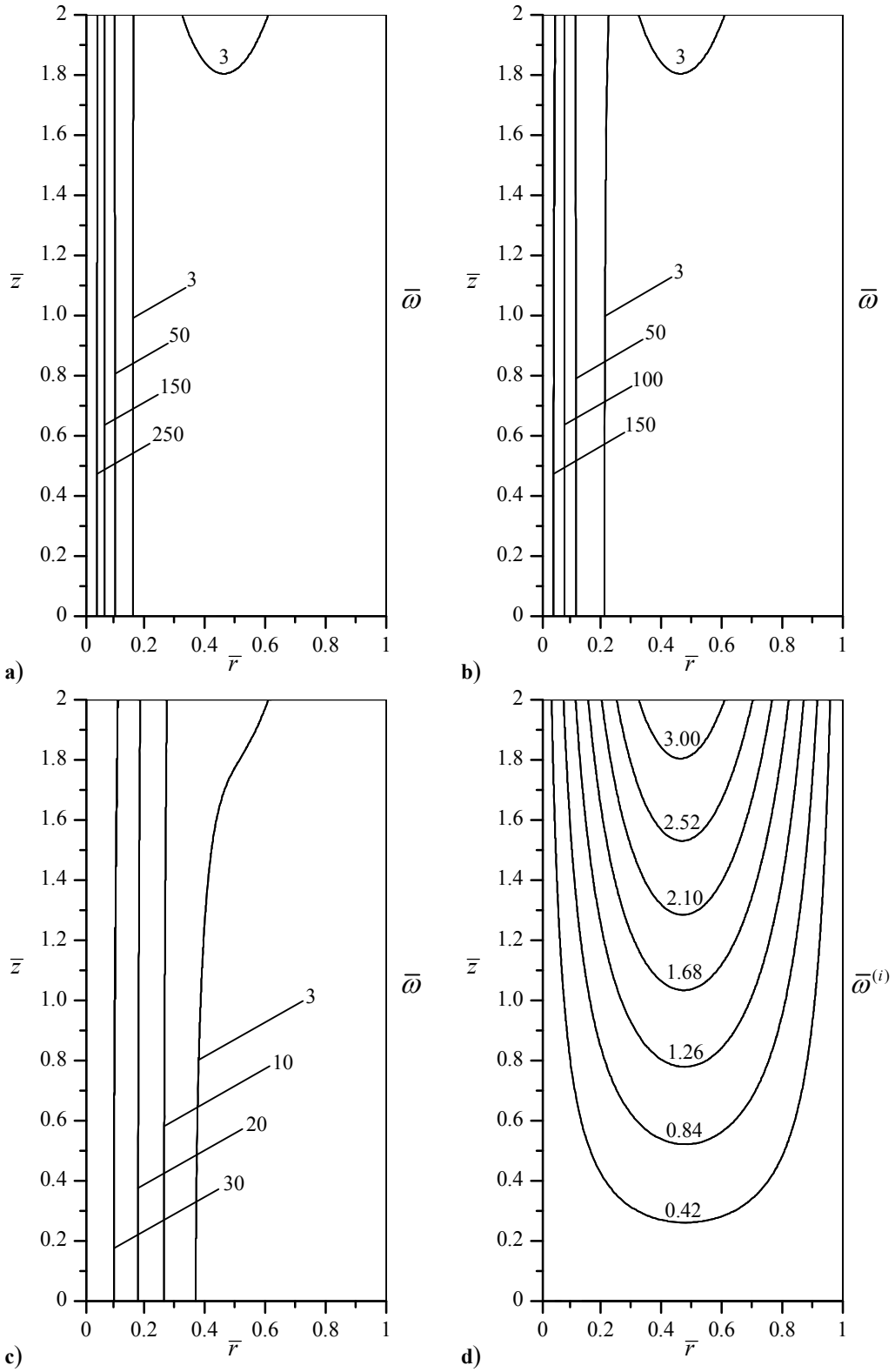

Figure 4. Vorticity distribution in a chamber for a Reynolds number of) 1000, b) 500, c) 100 and d) ∞ (inviscid flow). Results correspond to the linear Beltramian case with $l = 2$ and $\kappa = 0.125$.

Interestingly, we find that the vorticity generated in the viscous core markedly exceeds the one introduced into the chamber by the incoming fluid at the boundary by virtue of its swirling component in the inlet/outlet plane. Even for a low Reynolds number of, say, 100, the magnitude of the vorticity in the core will be approximately ten times larger than the one introduced into the chamber because of the rotational velocity imposed at the boundary. The maximum values of $\bar{\omega}$ in Figs. 4a, b, and c appear to be 100, 50 and 10 times larger than $\bar{\omega}$ in Fig. 4d, respectively. Furthermore, while $(\bar{\omega})_{\max}$ in Figs. 4a-c is generated around the centerline, $(\bar{\omega})_{\max}$ in Fig. 4d occurs at the endwall where flow is injected.

As the Reynolds number is lowered, the area where vorticity is generated expands, but the magnitude of the vorticity per unit volume decreases. It may also be seen that the vorticity remains confined to the core region and does not spread to the outer parts of the chamber. This is mainly due to the core region being envaginated by the inner vortex wherein the fluid is constantly spiraling while traveling towards the endwall before exiting the chamber.

It should also be noted that as the Reynolds number approaches infinity, the momentum forces will completely prevail over the entire domain. Viscous effects will become so small in comparison that, from a mathematical perspective, as $Re \to \infty$, Eqs. (38), (42) and (44) reduce to their inviscid analogs given by Eqs. (47), (48) and (46), respectively.

C. Rectified Pressure Distribution

The radial pressure gradient increases when moving away from the sidewall toward the centerline. This is due to the rapidly growing vacuum pressure as $\bar{r} \to 0$. In the inviscid case, a singularity is detected that causes the total pressure to reach absolute vacuum at the centerline. This behavior is illustrated in Fig. 5 where the role of viscosity is evident in reducing the pressure gradient near the core until it vanishes at $\bar{r} = 0$.

The companion Fig. 6 displays the variation of the total pressure in the vicinity of the core. In all cases considered, the pressure drops precipitously as it approaches the axis of the chamber, thus attaining its minimum at $\bar{r} = 0$. The Reynolds number appears to have a substantial impact on the variation of the pressure. Higher values of the Reynolds number signal the presence of larger differences between the sidewall and core pressures. At radial positions that correspond approximately to $\bar{r} > 0.15$, all pressure curves quickly converge to the same value as the inviscid solution.

The cases shown in Figs. 5 and 6 pertain to the linear Beltramian profile with a chamber aspect ratio of $l = 1$. Similar viscous core corrections can be applied to the complex-lamellar and the nonlinear Beltramian profiles although their analysis is omitted here.

Before leaving this subject, it may be helpful to remark that, so far, no exact analytical solution for the total pressure could be found, and this may be caused by intractable integrals that prevent the extraction of a closed-form solution. Instead, series approximations are used to solve those integrals and generate the requisite illustrations.

D. Sidewall Boundary Layer

In practice, the presence of friction and attendant boundary layers must be accounted for along the sidewall and headwall sections of the vortex chamber. These require the enforcement of no slip on all three components of velocity. Although friction significantly reduces the velocities near the walls, its impact remains limited to a narrow region. Figure 7 depicts the angular velocity measurements from a classic experiment by Smith.[18] In this setup, the viscous core region extends up to 26% of the chamber. In contrast, the sidewall boundary layer extends across a mere 7% of the radius.

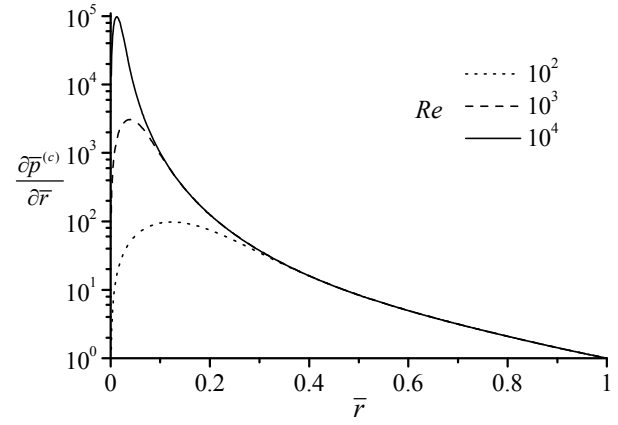

Figure 5. Radial variation of the pressure gradient at different Reynolds numbers.

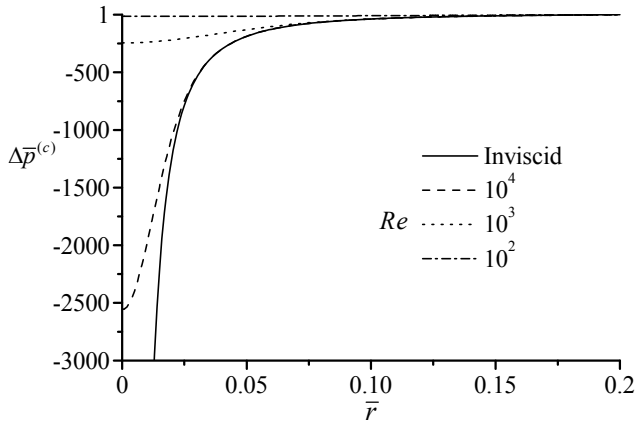

Figure 6. Pressure variation near the core of the vortex chamber for the inviscid and semi-viscous cases.

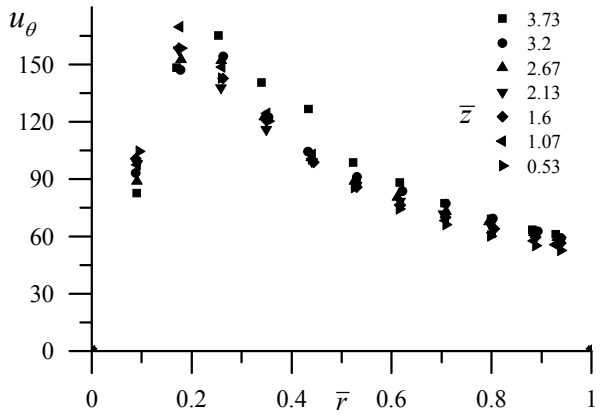

Figure 7. Experimental u_θ at different axial positions based on data extracted from Smith[18] using his Case 1.

The sidewall and headwall boundary layers are important for computing the shear stresses exerted on the walls; these can affect many calculations such as those concerned with stability, torques, losses, friction coefficients, etc. Their detailed characterization along with other flow features will be addressed in future work.

IV. Closing Remarks

In this study, a viscous boundary layer treatment near $\bar{r} = 0$ is applied to the inviscid solution by Akiki and Majdalani.[28] The ensuing approximation is devoid of singularities that once plagued the strictly inviscid tangential velocity and pressure. The rectified tangential velocity increases while approaching the centerline, reaches a maximum where viscous forces prevail, and then diminishes until it reaches zero at $\bar{r} = 0$. This component of velocity shows no dependency on the axial position in the core region when the *tangential momentum constant* $\bar{C}$, which is specified by the boundary condition on the tangential velocity, falls within the neighborhood of the first root of the Bessel function of the first kind.

The pressure behaves nearly identically to the inviscid solution in the outer region. It decreases as we move away from the sidewall, and, instead of reaching absolute vacuum at the centerline (cf. the inviscid solution), the pressure and its gradient decrease when viscous effects begin to escalate. At the outset, the total pressure reaches a finite minimum as $\bar{r} \to 0$. The low pressure near the centerline may be viewed as the driving force that causes the outer vortex to spiral toward the headwall, instead of spilling directly out of the nozzle/discharge port. An increase in *Re* will hence give rise to an increase in chamber pressure.

Before closing, it may be useful to remark that the viscous correction leads to the generation of vorticity within the core region. Here we show that the vorticity produced in the vortex chamber because of viscosity exceeds the vorticity that may be introduced through the inlet plane by the flow injection boundary condition. As the Reynolds number decreases, vorticity is generated inside a larger portion of the chamber that builds concentrically around the core. However, $\bar{\omega}$ remains confined to the inner vortex until exiting because of the axial velocity in the core region that is forcefully transporting mass in its continual downstream motion toward the endwall. Evidently, as $Re \to \infty$, the inviscid solution is restored. Finally, the aspect ratio of the chamber turns out to be an effective parameter to consider. As l increases, the viscous core region grows in diameter, thus leading to a wider spread of viscous effects.

Acknowledgments

This material is based on work supported partly by the National Science Foundation through Grant No. CMMI-0928762, and partly by the University of Tennessee Space Institute, through institutional cost sharing.

References

[1]Vatistas, G. H., "Vortices in Homer's Odyssey — a Scientific Approach," *Science and Technology in Homeric Epics,* Vol. 6, edited by S. A. Paipetis, Springer, The Netherlands, 2009, pp. 67-75.

[2]Gloyer, P. W., Knuth, W. H., and Goodman, J., "Overview of Initial Research into the Effects of Strong Vortex Flow on Hybrid Rocket Combustion and Performance," CSTAR Fifth Annual Symposium Paper N96-16953, January 1993.

[3]Knuth, W. H., Bemowski, P. A., Gramer, D. J., Majdalani, J., and Rothbauer, W. J., "Gas-Fed, Vortex Injection Hybrid Rocket Engine," NASA Marshall Space Flight Center, SBIR Phase I Final Technical Rept. NASA/MSFC Contract NAS8-40679, Huntsville, AL, August 1996.

[4]Chiaverini, M. J., Malecki, M. J., Sauer, J. A., Knuth, W. H., and Majdalani, J., "Vortex Thrust Chamber Testing and Analysis for O2-H2 Propulsion Applications," AIAA Paper 2003-4473, July 2003.

[5]Matveev, I., Matveeva, S., and Serbin, S., "Design and Preliminary Test Results of the Plasma Assisted Tornado Combustor," AIAA Paper 2007-5628, July 2007.

[6]Majdalani, J., "Exact Eulerian Solutions of the Cylindrical Bidirectional Vortex," AIAA Paper 2009-5307, August 2009.

[7]Rankine, W. J. M., *A Manual of Applied Mechanics*, 9th ed., C. Griffin and Co., London, UK, 1858.

[8]Oseen, C. W., "Über Wirbelbewegung in Einer Reibenden Flüssigkeit," *Arkiv för Matematik Astronomi och Fysik,* Vol. 7, No. 14, 1912, pp. 1-13.

[9]Lamb, H., *Hydrodynamics*, 6th ed., Cambridge University Press, Cambridge, UK, 1932.

[10]Batchelor, G. K., "Axial Flow in Trailing Line Vortices," *Journal of Fluid Mechanics,* Vol. 20, No. 4, 1964, pp. 645-658. doi: 10.1017/S0022112064001446

[11]Burgers, J. M., "On the Resistance of Fluids and Vortex Motion," *Proceedings of Koninklijke Nederlandse Akademie van Wetenschappen (KNAW),* Vol. 23, No. 1, 1921, pp. 774-782.

[12]Burgers, J. M., "A Mathematical Model Illustrating the Theory of Turbulence," *Advances in Applied Mechanics,* Vol. 1, 1948, pp. 171-199. doi: 10.1016/S0065-2156(08)70100-5

[13]Sullivan, R., "A Two-Cell Vortex Solution of the Navier-Stokes Equations," *Journal of the Aerospace Sciences,* Vol. 26, No. 11, 1959, pp. 767-768.

[14]Bloor, M. I. G., and Ingham, D. B., "The Flow in Industrial Cyclones," *Journal of Fluid Mechanics,* Vol. 178, No. 1, 1987, pp. 507-519. doi: 10.1017/S0022112087001344

[15]Barber, T. A., and Majdalani, J., "Exact Eulerian Solution of the Conical Bidirectional Vortex," AIAA Paper 2009-5306, August 2009.

[16]Batterson, J. W., Maicke, B. A., and Majdalani, J., "Advancements in Theoretical Models of Confined Vortex Fowfields," JANNAF Paper TP-2007-222, May 2007.

[17]Kelsall, D., "A Study of the Motion of Solid Particles in a Hydraulic Cyclone," *Transactions of the Institution of Chemical Engineers,* Vol. 30, 1952, pp. 87-103.

[18]Smith, J., "An Experimental Study of the Vortex in the Cyclone Separator," *Journal of Basic Engineering-Transactions of the ASME,* Vol. 84, No. 4, 1962, pp. 602-608.

[19]Smith, J., "An Analysis of the Vortex Flow in the Cyclone Separator," *Journal of Basic Engineering-Transactions of the ASME,* Vol. 84, No. 4, 1962, pp. 609-618.

[20]Hoekstra, A., Derksen, J., and Van den Akker, H., "An Experimental and Numerical Study of Turbulent Swirling Flow in Gas Cyclones," *Chemical Engineering Science,* Vol. 54, No. 13, 1999, pp. 2055-2065. doi: 10.1016/S0009-2509(98)00373-X

[21]Derksen, J., and Van den Akker, H., "Simulation of Vortex Core Precession in a Reverse Flow Cyclone," *AIChE Journal,* Vol. 46, No. 7, 2000, pp. 1317-1331. doi: 10.1002/aic.690460706

[22]Fang, D., Majdalani, J., and Chiaverini, M. J., "Simulation of the Cold-Wall Swirl Driven Combustion Chamber," AIAA Paper 2003-5055, July 2003.

[23]Rom, C. J., Anderson, M. H., and Chiaverini, M. J., "Cold Flow Analysis of a Vortex Chamber Engine for Gelled Propellant Combustor Applications," AIAA Paper 2004-3359, July 2004.

[24]Vyas, A., and Majdalani, J., "Exact Solution of the Bidirectional Vortex," *AIAA Journal,* Vol. 44, No. 10, 2006, pp. 2208-2216. doi: 10.2514/1.14872

[25]Majdalani, J., and Rienstra, S., "On the Bidirectional Vortex and Other Similarity Solutions in Spherical Coordinates," *Journal of Applied Mathematics and Physics (ZAMP),* Vol. 58, No. 2, 2007, pp. 289-308. doi: 10.1007/s00033-006-5058-y

[26]Majdalani, J., and Chiaverini, M. J., "On Steady Rotational Cyclonic Flows: The Viscous Bidirectional Vortex," *Physics of Fluids,* Vol. 21, No. 10, 2009, pp. 103603-15. doi: 10.1063/1.3247186

[27]Batterson, J. W., and Majdalani, J., "Sidewall Boundary Layers of the Bidirectional Vortex," *Journal of Propulsion and Power,* Vol. 26, No. 1, 2010, pp. 102-112. doi: 10.2514/1.40442

[28]Akiki, G., and Majdalani, J., "On the Bidirectional Vortex with Arbitrary Endwall Velocity," AIAA Paper 2010-6652, July 2010.

[29]Batterson, J. W., and Majdalani, J., "On the Viscous Bidirectional Vortex. Part 1: Linear Beltramian Motion," AIAA Paper 2010-6763, July 2010.

[30]Batterson, J. W., and Majdalani, J., "On the Viscous Bidirectional Vortex. Part 2: Nonlinear Beltramian Motion," AIAA Paper 2010-6764, July 2010.